Journal of Materials Research and Technology 35 (2025) 1596–1607

Contents lists available at ScienceDirect

Journal of Materials Research and Technology

journal homepage: www.elsevier.com/locate/jmrt

A holistic research based on RSM and ANN for improving drilling outcomes in Al–Si–Cu–Mg (C355) alloy

Şenol Bayraktar [a,*], Cem Alparslan [a], Nurten Salihoğlu [a], Murat Sarıkaya [b,c]

[a] Mechanical Engineering, Recep Tayyip Erdoğan University, Rize, Türkiye
[b] Department of Mechanical Engineering, Sinop University, Türkiye
[c] Faculty of Mechanical Engineering, Opole University of Technology, 45-758, Opole, Poland

ARTICLE INFO

Handling Editor: M Meyers

Keywords:
Al–Si alloy
Drilling
Machining
Built up-edge
Optimization
RSM
ANN

ABSTRACT

The unique properties of Al–Si-based alloys make them suitable for components that demand structural integrity and wear resistance. This study was conducted to investigate the microstructure, mechanical, and drilling properties of a commercial alloy belonging to the Al–Si casting alloy group and containing approximately 4.5–5.5% Si (Al–5Si–1Cu–Mg). Drilling experiments were conducted with an 8 mm uncoated HSS (High-Speed Steel) drill across a range of cutting speeds (*V*) and feed rates (*f*) while maintaining a consistent depth of cut (DoC) parameters. Microstructural analysis using optical microscopy and SEM identified key phases within the alloy, including α-Al, eutectic Si, β-Fe (β-Al_5FeSi), and π-Fe (π-$Al_8Mg_3FeSi_6$) inter-metallics. Statistical analyses of the effects of *V* and *f* on thrust force (*Fz*), surface roughness (*Ra*), and torque (*Mz*) were performed using Response Surface Methodology (RSM), Artificial Neural Networks (ANN), and Analysis of Variance (ANOVA). The ANOVA results highlighted the significance of both *V* and *f* on the measured outputs, with optimal performance observed at a *V* of 125 m/min and *f* of 0.05 mm/rev (confidence level: 95%, $P < 0.05$). Additionally, predictive models based on RSM and ANN were developed for *Fz, Ra*, and *Mz*.

1. Introduction

Technological developments have necessitated the need for light metals for the production of mechanical components in industry. Aluminum-silicon (Al–Si) alloys, which are among the light metals, are frequently used in commercial sectors such as automotive due to these alloys high fluidity, specific strength, low shrinkage in casting and good corrosion resistance. Since they provide advantages in reducing vehicle weight and improving fuel economy, their use in automotive applications such as pistons, cylinder heads and engine blocks is increasing day by day [1]. This trend highlights the growing importance of Al–Si alloys in the context of global efforts to reduce energy consumption and environmental impact in transportation. Research shows that a 10% weight reduction in cars decreases fuel expenditure by 8% and exhaust emissions by 4% [2]. These findings further underscore the relevance of improving the properties of Al–Si alloys for automotive applications.

Pure aluminum cannot be used as a final product in the industry because it does not meet the structural and mechanical properties required for direct use. Therefore, pure aluminum is alloyed with many elements such as silicon (Si), copper (Cu) and magnesium (Mg) to improve its strength and other properties. Adding elements i.e., Cu and Mg to Al–Si alloys develops mechanical and microstructure properties such as elevated strength, ductility and hardness. Recent studies have shown that alloying with these elements significantly enhances the material's performance under various loading conditions, making it suitable for demanding industrial applications. In the literature review, Mohamed and Samuel [3] investigated the impacts of Mg addition on the structure of Al–Si–Cu–Mg. They found that Mg addition reduced the porosity without causing any noticeable initial melting. They also reported that Mg content plays a significant role in defining the mechanical features and microstructural stability of the materials under different casting conditions. Callegari et al. [4] studied the impact of various alloying elements on the microstructure and mechanical properties of Al–Si based casting alloys including Al–Si–Cu–Mg. They found that the presence of Mg and Cu considerably increased the hardness and tensile strength by contributing to the creation of fine precipitates during the aging process. They also revealed that the proportions of these elements should be determined in a controlled manner to optimize the balance between strength and ductility in these alloys. Beroual et al. [5] researched the effects of heat treatment (HT) and Cu (0.3 wt%) and

* Corresponding author.
E-mail address: senol.bayraktar@erdogan.edu.tr (Ş. Bayraktar).

https://doi.org/10.1016/j.jmrt.2025.01.115
Received 6 November 2024; Received in revised form 3 January 2025; Accepted 15 January 2025
Available online 15 January 2025

Mg (0.6 wt%) additions on structure and mechanical features of Al–Si–Cu and Al–Si–Mg. They highlighted that the HT process, especially the solution treatment followed by aging, significantly improved the tensile strength and hardness of the materials. They found that the alloy with Mg additions exhibited 34% more age-hardening than the alloy with Cu additions. It was determined that the elemental additions increased the strength and reduced the brittleness of the alloys by reducing the formation of needle-like β-Fe phases. Zhou et al. [6] identified that the type and morphology of the precipitated phase at the nanoscale changed with the rise in Cu content in Al–9Si-0.5 Mg-xCu casting alloys, and the yield strength improved between 103 and 130 MPa due to the precipitation strength. It was specified that the strength and ductility properties of Al–9Si-0.5 Mg–2Cu improved after aging, and the elongation, yield and ultimate tensile strength were measured as 8.4%, 351 MPa and 442 MPa, respectively. Aziz et al. [7] worked the impacts of T5 and T6 HTs on structure and mechanical properties of Al–Si–Cu–Mg (commercial A 319) manufactured by thixoforming casting methods. They emphasized that structure of the cast alloy comprised of spherical α-Al, uniformly distributed Si particles, and fragmented intermetallics. It was observed that T5 HT had no important impact on the precipitate distributed throughout the eutectic phase and the Si particle microstructure, while with T6 they revealed that Al_2Cu phase precipitated in the fine equiaxed grain structure and Si particles became spherical and coarse.

Alparslan and Bayraktar [8] researched the structural and mechanical features of as-cast and T6 HTed Al–7Si-0.6 Mg and found that the structure of the as-cast material comprised of α-Al, primary Si, eutectic Al–Si, Al_5FeSi and π-AlSiMgFe phases and that these phases partially dissolved and became spherical with HT.

The machining of materials manufactured by the casting method before being used in the mechanical system (such as milling, turning, drilling, etc.) is necessary for precise surface quality and dimensional accuracy. At the same time, this process can make a significant contribution to the service life and operating performance of workpieces in mechanical systems. In machining operations, in addition to parameters such as *V*, *f* and DoC, cutting tool and coating material, and coolant are also important factors on machinability outputs. These factors are effective on experimental outputs such as cutting force (*F*), *Ra* and tool wear, which play a significant role in determining the machinability index of the material. By controlling these factors in machinability, ideal cutting conditions can be determined. Thus, the time and cost criteria in production, which affect the global competitiveness of enterprises, can be optimized. Al–Si based alloys are commonly subjected to drilling processes so that they can be used in engine blocks and equipment, especially in the automotive industry. Although the hole drilling process seems like a basic process, hole surface quality, geometric and dimensional tolerance play a significant role in the assembly of mechanical components and the performance of these components within the operating system. In these processes, experimental outputs that determine hole quality such as *Fz*, *Ra*, axial misalignment, circularity, burr formation and hole diameter vary depending on the process parameters. Therefore, to achieve maximum performance, it is important to control independent variables, to statistically reveal their effects on dependent variables and to model them mathematically. In the literature, Hariharan et al. [9] optimized the cutting parameters for minimum wear and maximum material removal rate and tool life in turning of Al–Si 4032 material with coated carbide cutters under dry and wet conditions using different *V*, *f* and DoC parameters according to full factorial experimental design. In dry conditions, optimum independent variables were determined as 2600 rpm, 0.0982 mm/rev and 0.9 mm for *V*, *f* and DoC, respectively, while for wet cutting conditions they were determined as 2676 rpm, 0.125 mm/rev and 0.9 mm, respectively. Alparslan and Bayraktar [10] investigated the machining features of as-cast and T6 HTed Al–7Si-0.6 Mg material in milling process with TiAlN coated carbide tool at different *V* and *f* and optimized the cutting parameters for minimum *F* and *Ra* using RSM. It was identified that the HTed alloy exhibited lower *F* and *Ra* compared to the as-cast alloy and the optimum parameters for minimum *F* and *Ra* were specified as 125 m/min and 0.04 mm/rev for *V* and *f*, respectively. Jing et al. [11] optimized the independent variables for minimum *Ra* and *Fz* by ANN, RSM and genetic algorithm (GA) in the precision milling of Al–50%Si alloy with cemented carbide end mills using different cutting parameters. They found that the prediction performance of ANN and RSM for *Ra* and *F* was 95.83% and 98.06%, respectively. Bhushan [12] estimated the tangential, feed and radial force by GA and RSM in the turning of AA7075/15 wt%SiC alloy produced by stir casting with carbide inserts using different cutting parameters. They revealed that GA gave close values to RSM in predicting the minimum tangential force, while it gave better results than RSM for minimum feed and radial force.

In order to provide maximum performance of workpieces used in mechanical systems, it is critical to determine their structural, mechanical and machining features in advance. This situation becomes more evident especially in workpieces that cannot be used directly after casting and require additional machining operations for geometric and dimensional stability. Although the machinability of Al–Si alloys has been extensively studied, the specific performance of Al–Si–Cu–Mg alloys under repeated thermal cycles, particularly in automotive applications, remains insufficiently addressed. Given the increasing demand for lightweight, high-performance materials in the automotive industry, this study focuses on Al–5Si–1Cu–Mg alloys, which exhibit promising properties under repeated thermal cycles. Therefore, this paper, which deeply examines the properties of Al–5Si–1Cu–Mg material in the as-cast condition, contributes to the literature in this field. Building on previous studies, the current research further explores how the addition of Mg impacts the material's performance in automotive applications, particularly under thermal stress. In the study, the minimum *Mz*, *Fz* and *Ra* values after drilling were optimized with RSM and ANN, and successful mathematical models were developed for the prediction of experimental results. In addition, the statistical importance of *V* and *f* on experimental results was determined at a confidence level of 95% with ANOVA, and a new perspective was brought to the literature.

2. Material and method

2.1. Specimens and drilling tests

In this study, Al–5Si–1Cu–Mg material was produced by sand casting technique. During the production of the alloy, the elemental components were melted at 700 ± 5 °C. This melt was poured into a sand mold with a prismatic and angled mold cavity and solidified at room temperature (Fig. 1). In the manufacturing of the Al–5Si–1Cu–Mg, 99.7% pure commercial Al as well as Si, Cu and Mg elements were employed. The chemical composition (wt.%) of produced material was confirmed with ICP-OES technique. Accordingly, the chemical composition is composed of the following components: Si: 4.5–5.5, Fe: <0.01–0.5, Cu: 1.10–1.50, Mn: <0.01–0.10, Mg: 0.45–0.65, Ni: <0.01–0.10, Zn: <0.01–0.05, Ti: <0.01–0.15 and Al: Balance. The phases forming the microstructure of the alloy were revealed by optical microscope, energy dispersive spectroscopy (EDS) and scanning electron microscope (SEM) analyses. As seen in Fig. 1, the preparation of the samples consists of technical properties of the mold, metallography, hardness, tensile and machining test samples. The cast prismatic part was machined in a universal milling machine and made ready for tensile and machinability tests. For metallographic studies, samples were arranged by traditional techniques including grinding and polishing processes and analyzed using microscopic techniques. Hardness tests were carried out with the Brinell technique (HB) with a 2.5 mm ball under a load of 62.5 kgf. Tensile tests were executed on samples with dimensions of M12 × 88 mm with an average deformation of $5.9x10^{-3}s^{-1}$ and a constant jaw speed of 0.25 mm/min. After the tensile tests, fracture surfaces were imaged with SEM. To determine the mechanical features of the alloy, hardness measurements were executed by taking fifteen measurements

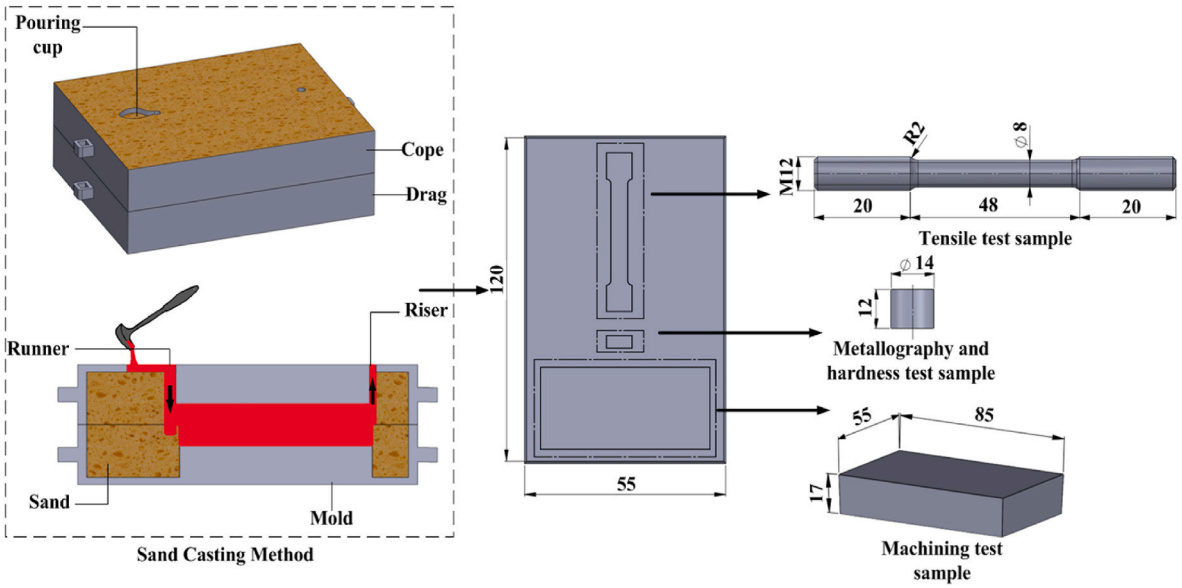

Fig. 1. Flow schema illustrating the arranging of the experimental specimens.

from each sample; elongation to fracture, yield and tensile strength values were calculated by taking the arithmetic average of the data obtained from three test specimens.

Then, drilling tests under dry conditions were performed on a CNC vertical machining center (Johnford VMC-850, 7.5 kW) with uncoated HSS drills, the technical properties of which are given in Table 1, at different cutting speeds (V: 75; 87.5; 100; 112.5 and 125 m/min), feed rates (*f*: 0.05; 0.10; 0.15; 0.20 and 0.25 mm/rev) and constant cutting depth (20 mm). *Fz*, *Mz* and *Ra* were measured as machinability outputs. Kistler 9257B dynamometer and Kistler 5070A amplifier were used for *Fz* and *Mz* measurement and Dynoware software was utilized to obtain data from graphics on the computer (Fig. 2).

Average *Ra* was determined using Mahr Perthometer M1 tracker-type equipment, taking into account the ISO 4287 standard. The *Ra* values were repeated five times at certain intervals around the 360° hole. The final *Ra* value was determined by the arithmetic average of five measurements.

2.2. Optimization of experimental outputs

2.2.1. RSM

RSM is a statistical method that uses mathematical models to ascertain how input and output variables relate to one another. In this technique, Face Centered-Central Composite Design was preferred, which allows the evaluation of quadratic relations between various input parameters together with linear effects [13]. In this study, three *V* (75, 100 and 125 m/min) and *f* (0.05; 0.15 and 0.25 mm/rev) were used as input variables as seen in Table 2, while experimental output variables were determined as *Fz, Mz* and *Ra*. As a result of the definition, quadratic mathematical models of experimental outputs were created as in Eq. (1). In this equation, *i, j, k* = 1, 2, 3 …. *n* and a_0, *bi*, *bij* and *bii* are the regression coefficients of the model, *Xi* and *Xj* are the explanatory variables and *Y* is the *Fz*, *Ra* and *Mz* outputs.

$$Y = a_0 + \sum_{i=1}^{k} b_i X_i + \sum_{ij}^{k} b_{ij} X_{ij} + \sum_{i=1}^{k} b_{ii} X_i^2 \quad (1)$$

in the last stage, mathematical models were developed for the prediction of experimental outputs according to Eq. (1). With ANOVA, the statistical importance of *V* and *f* input parameters on *Fz, Mz* and *Ra* output responses was determined at a 95% confidence level, taking into account the $P < 0.05$ criterion.

2.2.2. ANN

ANN is an estimation method frequently used in industrial applications to model complex relationships between input and output data sets. In this technique, outputs can be estimated for test parameter combinations by creating a model with input parameters and output data. ANN models provide effective solutions, especially in cases where it is difficult to determine process characteristics with empirical equations [14]. The structure of the ANN consists of a multilayer architecture consisting of an input layer, one or more hidden layers, and an output layer. The input and output layers have a set of neurons representing the variables of interest. Although there is no theoretical limit to the number of hidden layers, one or two layers are generally considered sufficient [15]. The output layer processes the information from the hidden layers and produces an output vector. Some research shows that single-output ANN models provide more successful results than multiple-output models [16,17]. The neurons in each layer are connected to each other with adjustable weights. These weights are optimized until errors are minimized during the training process. ANN offers ideal solutions for a specific problem by being trained with a suitable algorithm.

In this study, ANN modeling for *Fz, Mz* and *Ra* obtained in drilling of Al–5Si–1Cu–Mg alloy was performed using a subprogram in MATLAB software. Modeling process with ANN consists of two stages using training and test data. To minimize the error rate during the training process of the network, the input and output values given to the network were checked and in the test stage, the results were estimated according to the input values without changing the weight values. Based on experimental results, *Fz, Mz* and *Ra* values were analyzed separately using the generalized feed forward network structure. *V* and *f* variables were defined as input parameters, and *Fz, Mz* and *Ra* as output parameters. A total of 25 experiments were performed for each input parameter according to three levels. 18 out of 25 data were categorized for training and 7 for testing. The input and output data were transferred to

Table 1
Technical properties of drill.

Features	Value
Diameter (d1)	8 mm
Tip angle	118°
Shaft length (L1)	117 mm
Helix length (L2)	75 mm
Material and standard	HSS-DIN 338

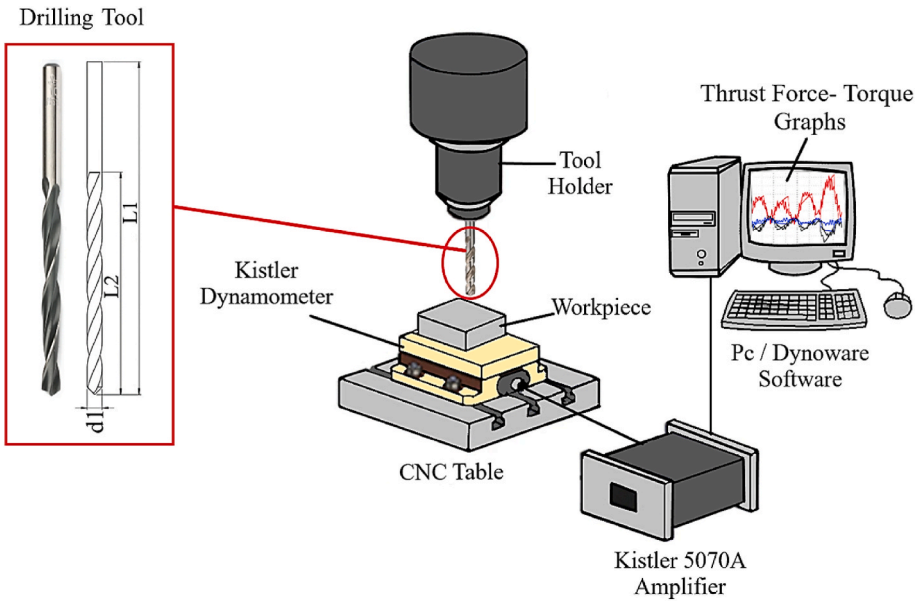

Fig. 2. Schematic arrangement of the experimental setup for measuring cutting forces.

Table 2
V and *f* parameters and its levels.

Level	*V* (m/min)	*f* (mm/rev)
−1	75	0.05
0	100	0.15
1	125	0.25

the software and the optimum network structures were determined by performing different experiments with these data (Fig. 3). During the training and testing process of the network, model performance was measured by Root Mean Square Error (RMSE) (Eq. (2)), while the evaluation of neural network model results was done by Mean Absolute Percentage Error (MAPE) (Eq. (3)) (N: number of data). The following

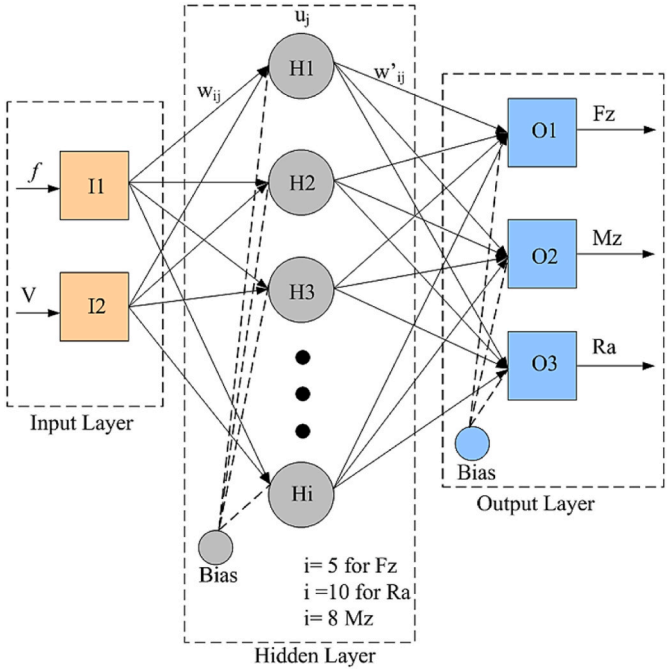

Fig. 3. The architecture of the neural network.

criteria were taken into account for MAPE values in the evaluation of the model: MAPE ≤10%: High accuracy, 10% < MAPE ≤20%: Good, 20% < MAPE ≤50%: Acceptable and MAPE >50%: Misleading prediction. The statistical significance and accuracy of the developed models were determined by the R^2 correlation coefficient (Eq. (4)).

$$RMSE = \sqrt{\frac{1}{N}\sum_{n=1}^{N}(Actual - Predicted)^2} \tag{2}$$

$$MAPE = \frac{1}{N}\sum_{n=1}^{N}\left(\frac{|Actual - Predicted|}{Actual}\right) \times 100 \tag{3}$$

$$R^2 = 1 - \left(\frac{\sum_{n=1}^{N}(Actual - Predicted)^2}{\sum_{n=1}^{N}(Predicted)^2}\right) \tag{4}$$

3. Results and discussion

3.1. Evaluation of experimental results

The microstructure of the alloy was carefully examined using optical and scanning electron microscopy (SEM) techniques, revealing a heterogeneous distribution of phases that play a critical role in the mechanical properties of the material. Semi-quantitative chemical compositions of the phases formed in the internal structure of the Al–5Si–1Cu–Mg alloy are given in Table 3. These compositions were determined using Energy Dispersive X-ray Spectroscopy (EDS), and the results were cross-checked with literature data to ensure accuracy [18, 19].

As seen in Fig. 4, the initial microstructure was characterized by distinct dendritic α-Al phases, which serve as the matrix, while the eutectic Si phase exhibited a fibrous morphology that is typical of Al–Si alloys. The presence of acicular β-Al5FeSi and π-Fe phases was also confirmed, which are known to influence the mechanical properties such as tensile strength and hardness.

As a result of tensile and hardness tests performed on Al–5Si–1Cu–Mg samples, the elongation to fracture, hardness, yield strength, and ultimate tensile strength were measured and found to be 1.8 ± 1%, 85 HB ±2, 140 ± 7, and 170 ± 10 N/mm^2, respectively. As

Table 3
Semi-quantitative chemical compositions of phases [18].

Phase	Al	Si	Fe	Cu	Mg	Mn
β-Al_5FeSi (Observed)	58.0–70.0	12.3–17.7	15.6–22.5	0.1–0.3	–	–
β-Al_5FeSi (In literature) [19]	45.2–75.8	5.2–15.0	17.9–35.0	–	–	–
π-(Observed)	57.4–87.1	7.8–23.3	2.2–15.0	1.4–5.5	2.3–7.5	0.4–1.9
π -(In literature) [19]	37.7–54.0	25.0–33.8	0.8–11.5	5.3–12.5	9.0–16.0	–

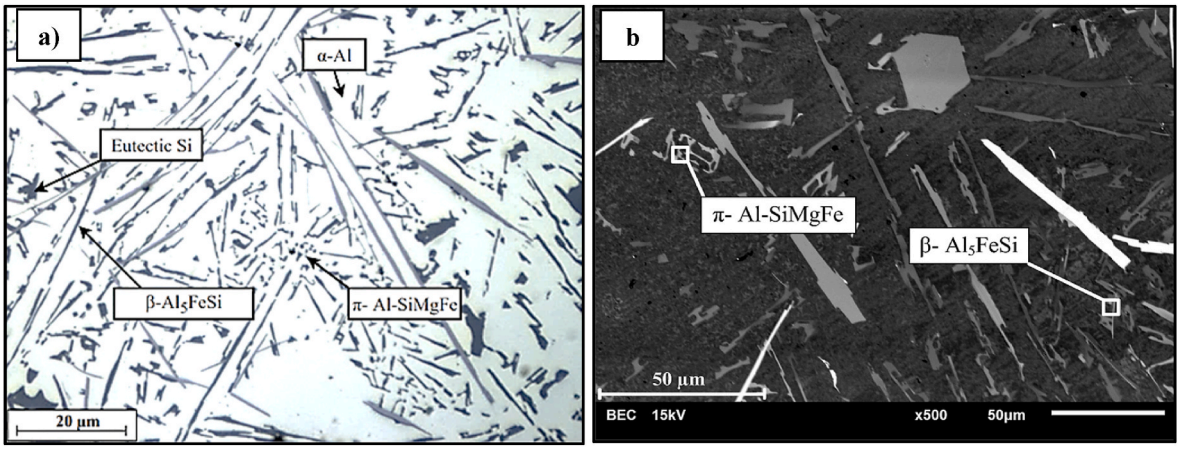

Fig. 4. The microstructure image of alloy, **a)** Optic microscope and **b)** SEM.

seen in Fig. 5, in addition to cleavage planes, pit and ridge-like structures were found on the fracture surfaces formed after the tensile tests. Furthermore, it was observed that wide surfaces and distinct microcracks were formed on the fracture surface. It was seen that the fracture continued along the dendritic boundaries. This suggests that the hard intermetallic phases, along with the Si particles, contributed to the initiation of the fracture, and the material's brittle nature was further accentuated by the presence of these phases.

As for the machinability test results, as presented in Fig. 6, it was observed that under constant *f* conditions, *Mz, Fz* and *Ra* reduced with rising *V* and increased with increasing *f*. It was determined that *Mz, Fz* and *Ra* decreased by 26.48, 6.71, 26.14% respectively, with the increase in *V* from 75 m/min to 125 m/min. With the effect of the increase in *V*, the temperature at the cutting tool-chip and workpiece interfaces increases in the deformation zones. It is thought that the yield strength of the cut material decreases, and it is more easily exposed to plastic deformation due to this temperature increase [20,21]. As a result, the cutting process becomes easier, lower forces occur, and *Fz* and *Mz* decrease. In alloys containing high amounts of Al, *Ra* generally decreases with increasing *V*. This situation is thought to be due to two different reasons. The first of these is that the cutting tool-workpiece contact occurs in a shorter period of time, and the other is that the resistance of the material against the cutting tool decreases due to the effect of high temperature. Thus, a more stable and sensitive surface can be obtained [10]. In other words, the workpiece surface temperature increases due to the increase in *V*. It is thought that this temperature improves the surface quality processed during drilling by softening the metallic bond of the material due to the lower resistance of the material to the cutting tool [22].

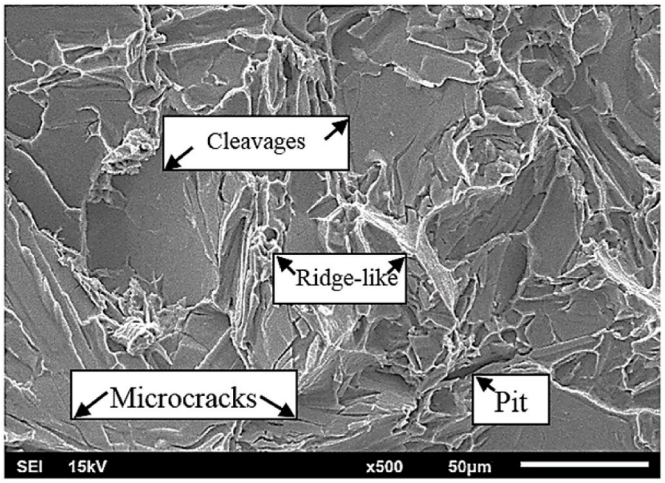

Fig. 5. Fractured surface of SEM image.

It was found that the *Mz, Fz* and *Ra* values increased by 9.38%, 2.70% and 16.84%, respectively, as the *f* increased from 0.05 mm/rev to 0.25 mm/rev at a constant *V* of 75 m/min (Fig. 7a). The same *f* increment showed that *Mz, Fz* and *Ra* increased by 101.57%, 125.71% and 41.60% at 87.5 m/min speed (Figs. 7b), 117.13%, 142.59% and 42.24% at 100 m/min speed (Figs. 7c), 123.88%, 114.67% and 94.45% at 112.5 m/min speed (Figs. 7d) and 98.67%, 157.61% and 66.22% at 125 m/min speed (Fig. 7e). With the increase in *f*, friction increases due to the increase in material removal rate per unit time [22] and the contact surface area at the tool-chip interface. As a result, more *Fz* and *Mz* are required for the cutting tool to resist shear stress [10]. Also, due to the increasing friction due to the progress, pitting or feed marks occur on the machined surface and the *Ra* increases [22]. In addition, the material removal rate (MMR) increases with the effect of increasing feed during cutting. It is thought that this increases *Ra* by increasing deflection and vibration in the tool.

During the machining of ductile materials containing high amounts of Al, the α-Al phase is smeared onto the cutting-edge rake face under the influence of thermal and mechanical stresses, causing the formation of a built-up layer (BUL) in the first stage [23]. As a result of the accumulation of smear formation on the rake face, a built-up edge (BUE) is formed. During cutting, BUE starts to act like a cutting edge and disrupts the cutting tool geometry. This causes friction on the workpiece rather than the cutting process, increasing the *F* and *Ra* [20]. In this study, the highest BUE formation on the cutting-edge during drilling occurred at *V* of 75 m/min and *f* of 0.25 mm/rev parameters (Fig. 8a), while lowest

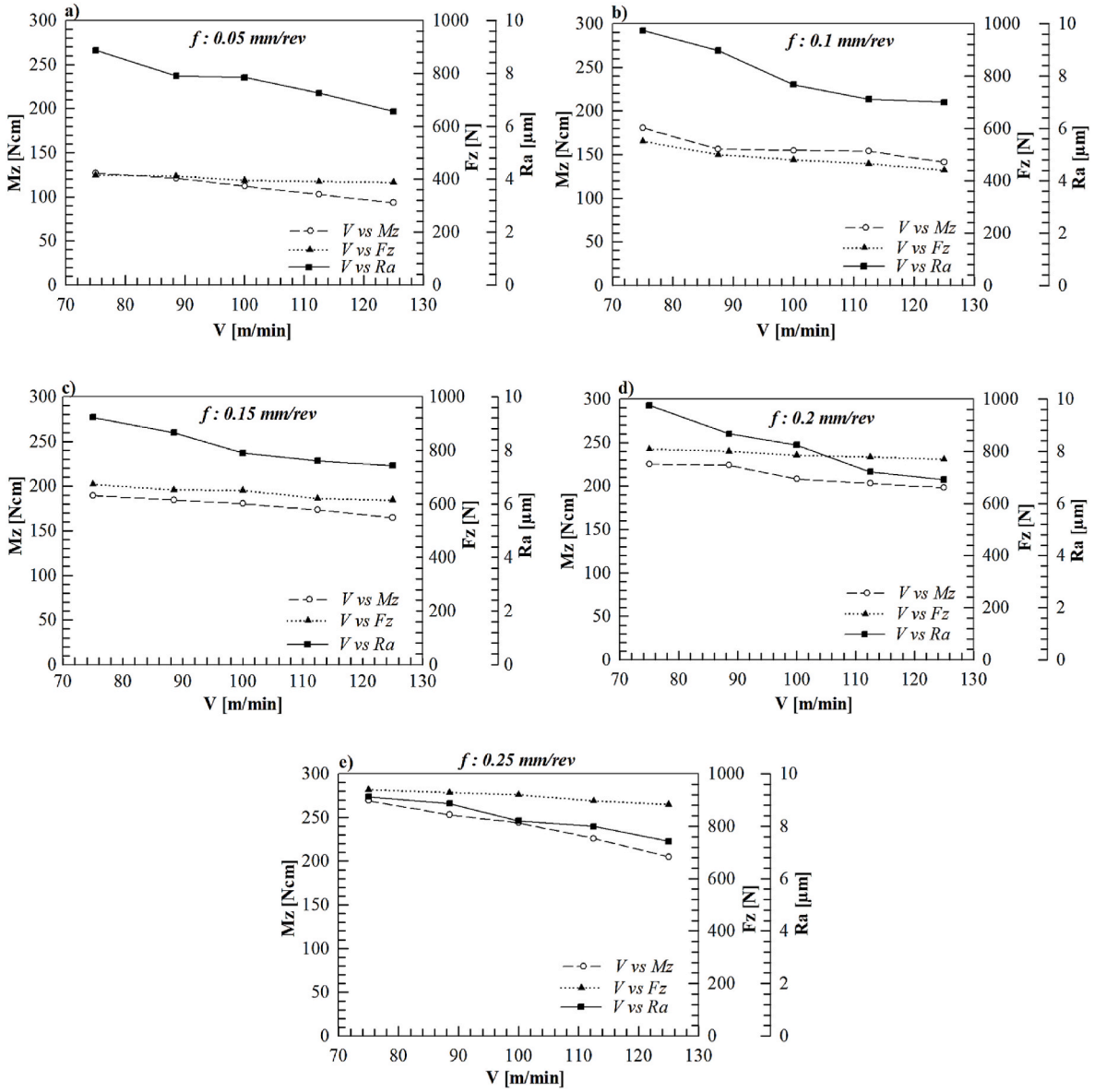

Fig. 6. Impact of variation in *V* on *Fz*, *Ra* and *Mz* at constant *f* values, a) 0.05 mm/rev, b) 0.10 mm/rev, c) 0.15 mm/rev, d) 0.20 mm/rev and e) 0.25 mm/rev.

occurred at *V* of 125 m/min and *f* of 0.05 mm/rev parameters (Fig. 8d). It was determined that BUE decreased with the increase in *V*, while it increased with the increase in feed rate (Fig. 8). Depending on the increase in *V*, the temperature in the primary cutting zone increases and the yield strength of cut material reduces with the effect of this temperature. Thus, BUE decreases on the cutting tool and the machined surface, and the machined surface quality is improved [24]. As the *f* increases, the amount of chip removed per unit time increases, causing the friction surface area at the cutting tool and chip interface to increase [25]. In tools having low thermal conductivity and diffusion rate, heat transfer slows down, causing heat accumulation at the tool-chip interface. This heat accumulation increases the BUE formation on the rake face leading to increased *F* and *Ra* [26]. When Fig. 8 is examined, it was seen that the composition of the layer adhering to the cutting edge is largely composed of Al due to thermomechanical factors. In other words, due to the compression forces, a large proportion of pure Al is swept away at the rake face by elements such as Si, Cu and Mg with high melting points in the alloy structure (Fig. 8-Energy-dispersive x-ray spectrometry A and B). These elements play a role as carriers of pure Al, increasing the BUE on the cutting tool and machined surface, thus increasing the *F* and *Ra* [20]. It was seen that spring type chip was formed during drilling. Scratches, serration, cracks and perforation occurred on the chips. It was observed that a brittle and short chip structure was formed due to the increase in *V* as provided in Fig. 8. This shows that saw-toothed continuous fragmented chip was formed during cutting. In machining, short chip formation is desired to obtain better machined surface quality. With short chip, chip evacuation from the cutting area becomes easier and can be removed quickly. At high *V* values, chips are mostly separated into segments and some continuous regions in the chip are blended. It has been shown in the literature that the change in the microstructure of the material under the effect of high temperature and the microstructure have a significant effect on chip formation during high-speed cutting in continuous and interrupted cutting conditions [27].

During drilling, the Si particles in the microstructure can be broken due to the friction between the cutting tool and the workpiece. Then, these particles spread over the machined surface. As a result of the movement of the broken particles with the ductile α-Al phase, voids may have formed on the machined surface, causing an increase in *Ra* [28]. In other words, Si fragmentation occurs due to plastic flow, compressive

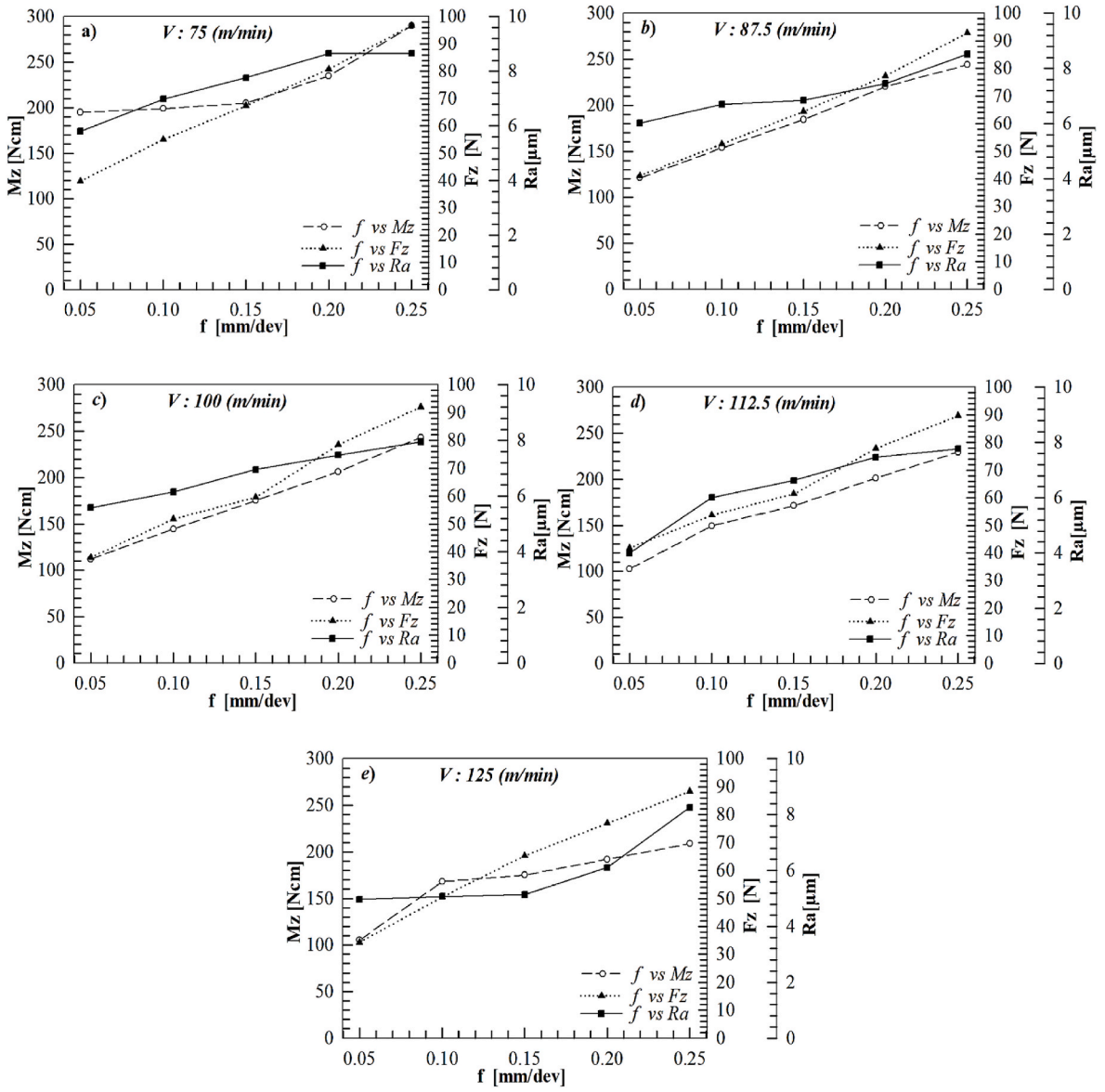

Fig. 7. Impact of variation in *f* on *Fz*, *Mz* and *Ra* at constant *V* values, a) 75 m/min, b) 87.5 m/min, c) 100 m/min, d) 112.5 m/min and e) 125 m/min.

stress, and cutting edge-silicon particle contact. It was observed that fragmented Si particles concentrated in the region close to the machined surface due to the effect of this fragmentation were distributed under the surface. The contact of Si particles with the drill during drilling causes damage to the particles, cracks and fractures in the primary Si particles. As a result of the movement of broken particles, cavities may occur on the machined surface. It is thought that these microstructural defects formed on the machined surface increase the surface roughness [28]. As mentioned before, it was seen that the *Ra* value reduced with the increase in *V*, and this situation is more clearly revealed by the machined subsurface images in Fig. 9. It is thought that the surface machined at high *V* has a more stable and smooth structure, which is due to less BUE formation on the cutting tool and the machined surface during cutting [29–32].

3.2. Statistical analysis

Based on the experimental design with RSM, the *Fz*, *Ra* and *Mz* values obtained during the drilling of the alloy are presented in Table 4. The statistical effects of input parameters *V* and *f* on *Fz*, *Ra* and *Mz* with ANOVA analysis are shown in Tables 5–7, respectively. Accordingly, it was determined that the binary interaction of *V*, *f* and *f*f* on *Fz* (Table 5), the interaction of *V*, *f* and *V*V* on *Ra* (refer to Table 6) and the variables *V* and *f* on *Mz* (refer to Table 7) were statistically significant.

Correlation coefficients (R^2) were calculated as 99.93%, 96.20% and 98.68% for *Fz*, *Ra* and *Mz*, respectively. These high coefficients demonstrate that the experimental results have a significant impact on the performance of the modeling. The quadratic formulas used in the determination of *Fz*, *Ra* and *Mz* with respect to input variables are presented in Eqs. (5)–(7), respectively.

$$Fz = 268.5 + 0.89V + 2564f - 0.00715\,V^2 + 953\,f^2 - 2.80\,V \times f \quad (5)$$

$$Ra = 17.34 - 0.1563V - 2.33f + 0.000531\,V^2 - 2.3\,f^2 + 0.0780\,V \times f \quad (6)$$

$$Mz = 41.1 + 1.08V + 1057f - 0.00719\,V^2 - 359\,f^2 - 3.06\,V \times f \quad (7)$$

in the optimization process performed with RSM, the minimum goal function was used for *Fz*, *Ra* and *Mz*. The lower and upper limits of the dependent and independent variables are given in Table 8. According to the experimental results obtained, the optimum cutting parameters for

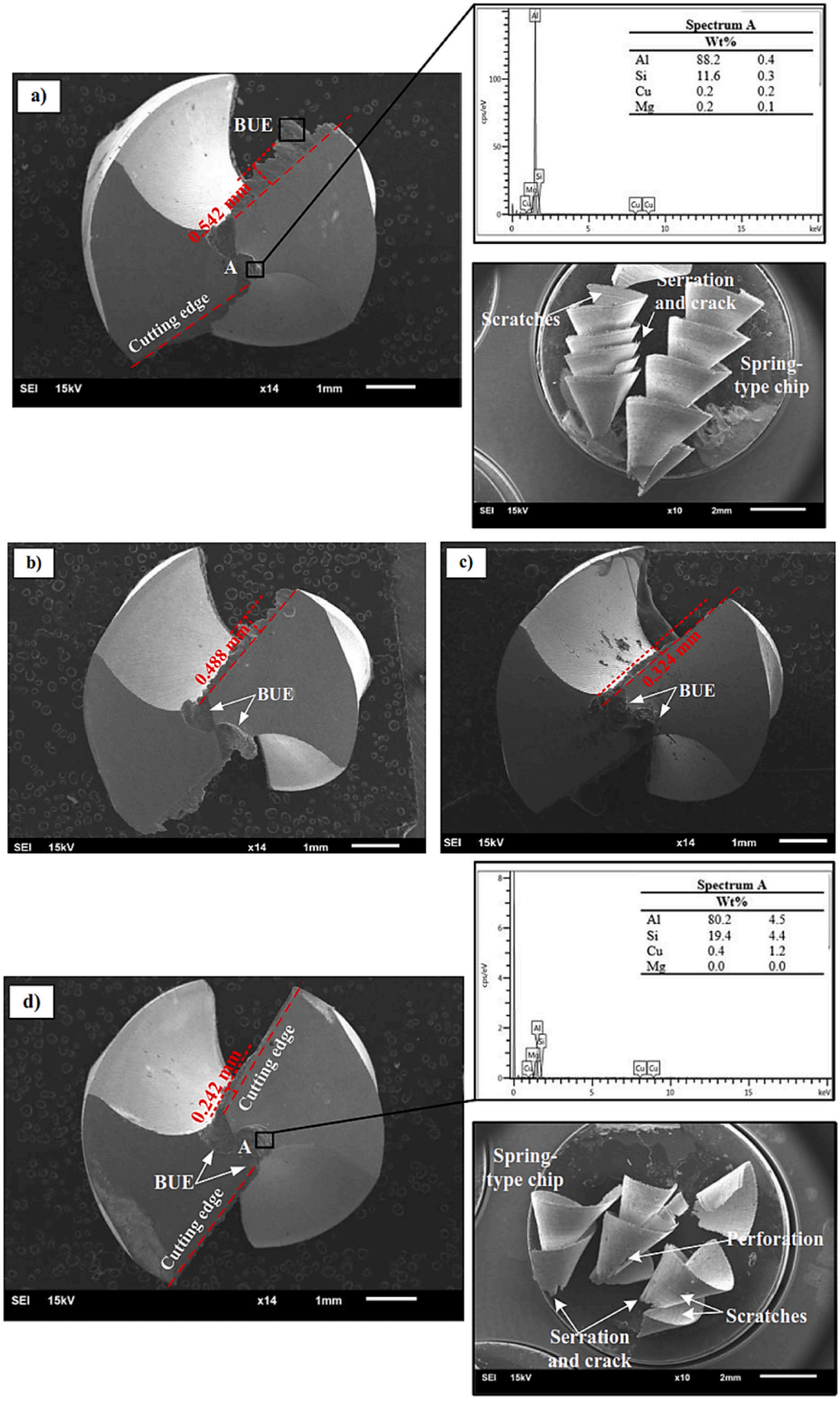

Fig. 8. SEM images of the cutting tool and chips, a) *V*: 75 m/min, *f*: 0.25 mm/rev, b) *V*: 75 m/min, *f*: 0.05 mm/rev, c) *V*: 125 m/min, *f*: 0.25 mm/rev and d) *V*: 125 m/min, *f*: 0.05 mm/rev.

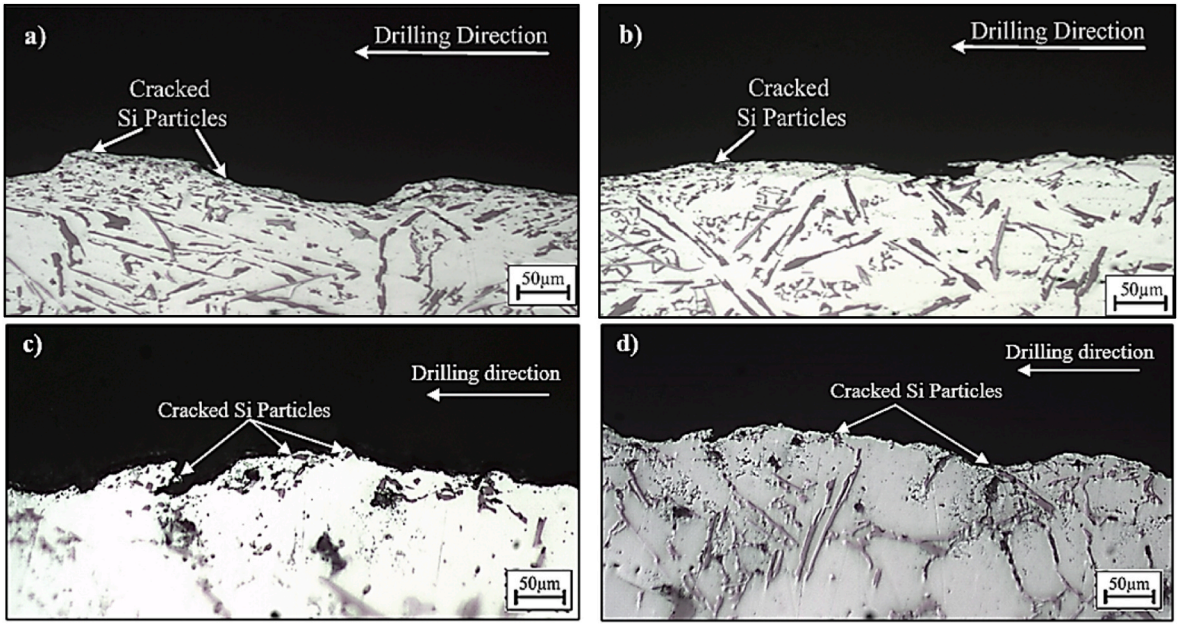

Fig. 9. Machined subsurface images in drilling of alloys, (a) *V*: 75 m/min, *f*: 0.05 mm/rev, (b) *V*: 125 m/min, *f*: 0.05 mm/rev, (c) *V*: 75 m/min, *f*: 0.25 mm/rev and (d) *V*: 125 m/min, *f*: 0.25 mm/rev.

Table 4
Experimental results measured for casted alloy.

Experimental number	Input parameters		Output parameters		
	V (m/min)	*f* (mm/rev)	*Fz* (N)	*Ra* (µm)	*Mz* (Ncm)
1	75	0.05	416	8.87	126.9
2	125	0.05	388	6.55	93.30
3	100	0.15	651	7.9	180.4
4	75	0.25	939	9.42	269.2
5	125	0.25	883	7.88	205.0
6	100	0.15	648	7.91	176.3
7	100	0.15	654	8.02	188.2
8	100	0.15	657	7.99	189.5
9	100	0.05	396	7.21	112.1
10	75	0.15	674	9.01	189.5
11	100	0.15	645	7.42	176.2
12	100	0.15	646	7.34	179.3
13	125	0.15	614	7.11	164.6
14	100	0.25	920	8.20	243.8

Table 5
ANOVA table for *Fz*.

Source	Df	SS	MS	F	P	Observation
Model	6	400249	66708	1603.14	0.000	Sig.
Blocks	1	18	18	0.43	0.533	Insig.
Lineer	2	399750	199875	4803.43	0.000	Sig.
V	1	3456	3456	83.06	0.000	Sig.
f	1	396294	396294	9523.81	0.000	Sig.
Square	2	251	126	3.02	0.114	Insig.
*V***V*	1	54	54	1.31	0.290	Insig.
*f***f*	1	248	248	5.96	0.045	Sig.
2-Way interaction	1	196	196	4.71	0.067	Insig.
*V***f*	1	196	196	4.71	0.067	Insig.
Error	7	291	42	–	–	–
Lack of fit	3	185	62	2.31	0.218	Insig.
Pure error	4	107	27	–	–	–
Total	13	400540	–	–	–	–

Abbreviation: Sig.: Significant, InSig.: Insignificant, Df: Degree of freedom, SS: Sum of square, MS: Mean of square.
R^2: 99.93%, R^2 (Adj): 99.86% R^2 (Pred): 99.35%.

Table 6
ANOVA table for *Ra*.

Source	Df	SS	MS	F	P	Observation
Model	6	7.753	1.292	29.55	0.000	Sig.
Blocks	1	0.172	0.172	3.93	0.088	Insig.
Lineer	2	6.902	3.451	78.92	0.000	Insig.
V	1	5.529	5.529	126.45	0.000	Sig.
f	1	1.372	1.372	31.39	0.001	Sig.
Square	2	0.330	0.165	3.78	0.077	Insig.
*V***V*	1	0.300	0.300	6.87	0.034	Sig.
*f***f*	1	0.001	0.001	0.03	0.861	Insig.
2-Way interaction	1	0.152	0.152	3.48	0.104	Insig.
V**f*	1	0.152	0.152	3.48	0.104	Insig.
Error	7	0.306	0.043	–	–	–
Lack of fit	3	0.045	0.015	0.24	0.868	Insig.
Pure error	4	0.260	0.065	–	–	–
Total	13	8.059	–	–	–	–

R^2: 96.20%, R^2 (Adj):92.95 % R^2 (Pred): 92.00%.

Table 7
ANOVA table for *Mz*.

Source	Df	SS	MS	F	P	Observation
Model	6	27704.9	4617.5	87.44	0.000	Sig.
Blocks	1	0.0	0.0	0.00	0.986	Insig.
Lineer	2	27311.8	13655.9	258.60	0.000	Sig.
V	1	2511.3	2511.3	47.56	0.000	Sig.
f	1	24800.5	24800.5	469.64	0.000	Sig.
Square	2	140.8	70.4	1.33	0.323	Insig.
*V***V*	1	55.0	55.0	1.04	0.341	Insig.
*f***f*	1	35.2	35.2	0.67	0.441	Insig.
2-Way interaction	1	234.9	234.9	4.45	0.073	Insig.
*V***f*	1	234.9	234.9	4.45	0.073	Insig.
Error	7	369.7	52.8	–	–	–
Lack of fit	3	199.7	66.6	1.57	0.329	Insig.
Pure error	4	169.9	42.5	–	–	–
Total	13	28074.6	–	–	–	–

R^2: 98.68%, R^2 (Adj): 97.55% R^2 (Pred): 89.56%.

Table 8
Goal and independent variables for optimization of *Fz*, *Ra*, and *Mz*.

Variables	Goal	Lower limit	Upper limit	Weight	Significance
V (m/min)	Limit range	75	125	1	1
f (mm/rev)	Limit range	0.05	0.25		
Fz (N)	Minimum	388	939		
Ra (μm)	Minimum	6.55	9.42		
Mz (Ncm)	Minimum	93.3	269.25		

the minimum *Fz, Ra* and *Mz* values with RSM were calculated as *V*: 125 m/min and *f*: 0.05 mm/rev. It was found that the error rate between the mathematical model results obtained in the optimum parameters and the experimental results varied between 1.38% and 6.71%, and these low error rates showed that the optimization process was successfully performed is indicated in Table 9. In addition, the optimum input variables for *Fz, Ra* and *Mz* and the response and desirability values are presented in Table 10. It is observed that the optimum *V* and *f* to reach the minimum *Fz, Ra* and *Mz* values are 125 m/min and 0.05 mm/rev, respectively.

After the alloy drilling process was completed, estimated mathematical models were developed for *Fz, Ra* and *Mz* values using ANN. In the modeling process, the independent variables of *V* and *f* were defined as inputs, and *Fz, Ra* and *Mz* were assigned to the output layer as dependent variables. A single hidden layer was used in all network structures, and the number of neurons was structured differently for each model. While tansig-purelin activation functions and Scaled Conjugate Gradient Backpropagation Algorithm (trainscg) learning algorithm were preferred in modeling *Fz*, purelin-purelin activation function and Newton backpropagation (trainbfg) learning algorithm were used for *Ra* and *Mz*. The most suitable network structure for *Fz* was determined as 2-5-1, for *Ra* as 2-10-1 and for *Mz* as 2-8-1. Weight and threshold values, activation functions and learning algorithms are presented in Tables 11–13, respectively, and the mathematical models obtained for *Fz, Ra* and *Mz* based on these values are given in Eqs. (8)–(10).

$$F_i = \frac{2}{1+e^{-2\left[f.W_{fFi}+V.W_{VFi}+\theta i\right]}} - 1 \tag{8}$$

$$Fz = \sum_{i=1}^{5} F_i.W_i + \theta_j \tag{9}$$

$$Fz = \sum_{i=1}^{5} \left(\frac{2}{1+e^{-2\left[f.W_{fFi}+V.W_{VFi}+\theta i\right]}} - 1 \right).W_i + \theta_j \tag{10}$$

The mathematical models obtained for *Ra* according to the weight and threshold values are given in Eqs. (11)–(13).

$$F_i = f.W_{fFi} + V.W_{VFi} + \theta i \tag{11}$$

$$Ra = \sum_{i=1}^{10} F_i.W_i + \theta_j \tag{12}$$

$$Ra = \sum_{i=1}^{10} \left(f.W_{fFi} + V.W_{VFi} + \theta_i \right).W_i + \theta_j \tag{13}$$

The mathematical models obtained for *Mz* according to the weight and threshold values are given in Eqs. (14)–(16).

$$F_i = f.W_{fFi} + V.W_{VFi} + \theta i \tag{14}$$

$$Mz = \sum_{i=1}^{8} F_i.W_i + \theta_j \tag{15}$$

$$Mz = \sum_{i=1}^{8} \left(f.W_{fFi} + V.W_{VFi} + \theta_i \right).W_i + \theta_j \tag{16}$$

in the network structures created with ANN, the RMS, MAPE and R^2 values for the *Fz, Ra* and *Mz* outputs are presented in Table 14. When the obtained results are examined, it was determined that the R^2 values are between 0.9974 and 0.9993, and the MAPE values are between 0.8887 and 2.4432. These values indicated that the error rate in the estimation of experimental data is below 5% and that ANN models can predict the results with high accuracy.

Lastly, the experimental results (*Fz, Ra* and *Mz*) obtained as a result of the drilling tests were compared with RSM and ANN techniques and the prediction performances of these techniques depending on the error rates of the mathematical models created were analyzed (Table 15). According to the evaluations, while the error rates of RSM in estimating

Table 9
Comparison of experimental and optimum results.

Output Parameter	*V (m/min)*	*f (mm/rev)*	Experimental result	Optimum response	Error (%)
Fz (N)	125	0.05	388	381.11	−1.77
Ra(μm)			6.55	6.459	−1.38
Mz (Ncm)			103.4	96.461	−6.71

Table 10
Independent variable parameters and its optimum values.

V (m/min)	*f (mm/rev)*	Optimum value, *Fz (N)*	Optimum value, *Ra (μm)*	Optimum value, *Mz (Ncm)*	Desirability
125	0.05	381.11	6.459	96.461	0.994

Table 11
Weight and threshold values for each neuron in *Fz*.

i	W_1	W_2	θ_i	L_w	θ_6
1	27.94961	−0.21327	−1.68524	−1.62185	1.612066
2	30.31877	−0.11817	−9.2325	−1.61693	–
3	−13.8773	0.296776	−9.14043	1.620129	–
4	15.40204	−0.00442	−0.90565	1.640512	–
5	17.51585	−0.0081	−2.80913	1.630368	–

Table 12
Weight and threshold values for each neuron in *Ra*.

i	W_1	W_2	θ_i	L_w	θ_{11}
1	−0.92051	0.06748	−1.90771	−2.0522	0.936473
2	−0.66138	−0.58777	−1.31878	−1.327	–
3	−0.16174	−0.57097	1.306212	1.3529	–
4	1.11969	−0.46266	−0.1569	−0.521	–
5	0.856703	0.449379	0.377925	0.7617	–
6	0.214264	0.506652	−0.97467	−0.7696	–
7	0.692709	−0.09152	1.043225	1.1351	–
8	−0.29605	−0.6844	−0.57075	−0.5644	–
9	−0.80074	0.567302	0.467193	−0.2831	–
10	0.380636	0.293331	−0.61387	−0.7539	–

Table 13
Weight and threshold values for each neuron in *Mz*.

i	W_1	W_2	θ_i	L_w	θ_9
1	2.948136745	−0.408331819	−1.34252	3.919242	9.295644
2	3.377475489	0.588057859	−1.54713	4.129223	–
3	14.45539596	−0.893356624	0.240263	15.28315	–
4	−16.63434383	−0.565373654	−7.99395	−13.3967	–
5	2.743026783	0.71975661	7.418378	−0.96517	–
6	−1.687985708	0.24353408	1.341268	−3.11595	–
7	11.65639883	0.879353442	6.912928	8.738089	–
8	−2.529769245	0.31465355	3.546087	−4.69264	–

Table 14
RMSE, MAPE and R^2 values for training and testing datas in *Fz*, *Ra* and *Mz*.

Type	RMSE	MAPE	R^2
Fz (N)			
ANN Training Data	4.9691	0.8887	0.9993
ANN Test Data	9.6545	1.0325	0.9987
Ra (μm)			
ANN Training Data	0.1469	1.4237	0.9852
ANN Test Data	0.1257	1.5504	0.9977
Mz (Ncm)			
ANN Training Data	3.6084	2.2832	0.9974
ANN Test Data	4.9643	2.4432	0.9974

Table 15
Experimental, RSM, ANN results and error rates in different cutting parameters.

Cutting Parameters	RSM			ANN	
	Fz (N)				
V (m/min); *f* (mm/rev)	Experimental result	Model result	Error rate (%)	Model result	Error rate (%)
87.5; 0.05	412	409.06	0.71	407.06	1.19
125; 0.05	388	380.21	2.00	387.08	0.23
100; 0.1	520	522.13	0.40	522.89	0.55
75; 0.15	674	666.87	1.05	669.52	0.66
112.5; 0.15	620	634.22	2.29	635.09	2.43
87.5; 0.2	800	789.95	1.25	799.79	0.02
125; 0.2	769	745.35	3.07	748.57	2.65
100; 0.25	920	912.06	0.86	913.45	0.71
Ra (μm)					
87.5; 0.05	7.90	8.109	2.44	8.06	1.95
125; 0.05	6.55	6.77	3.41	6.68	1.99
100; 0.1	7.66	7.48	2.33	7.77	1.30
75; 0.15	9.01	9.55	5.99	9.76	1.31
112.5; 0.15	7.61	7.46	1.90	7.67	0.87
87.5; 0.2	8.67	8.39	3.16	8.76	1.10
125; 0.2	7.26	7.04	1.95	7.03	1.83
100; 0.25	8.20	7.89	3.76	8.27	2.12
Mz (Ncm)					
87.5; 0.05	121.10	119.11	1.63	123.58	2.05
125; 0.05	93.30	98.41	4.81	107.93	4.38
100; 0.1	181.80	148.71	3.93	149.64	3.32
75; 0.15	189.50	197.70	4.32	191.86	1.24
112.5; 0.15	183.40	170.43	1.70	172.71	0.39
87.5; 0.2	226	224.04	0.86	214.42	4.27
125; 0.2	198.30	192.29	3.02	195.77	1.27
100; 0.25	243.80	242.51	0.52	237.48	2.58

Fz, Ra and *Mz* varied in the range of 0.40–3.07%, 1.90–5.99% and 0.52–4.81%, respectively; the error rates of ANN in the predictions were determined to be in the range of 0.02–2.43% for *Fz*, 0.87–2.12% for *Ra* and 0.39–4.38% for *Mz*. Considering these results, it was seen that ANN had higher prediction performance compared to RSM.

4. Conclusion

In this study, the structural, mechanical and machininig properties of the Al–5Si–1Cu–Mg material manufactured by sand casting technique were investigated comprehensively. The results of the machinability tests were evaluated on parameters i.e., *Fz*, *Ra* and *Mz*, and these experimental data were analyzed with RSM and ANN techniques to create mathematical models. Moreover, the impacts of input factors i.e., *V* and *f* rate on machinability indicators were statistically evaluated via ANOVA analysis. The main results obtained from the study are summarized below.

- The structure of the material consists of aluminum-rich α-Al matrix, eutectic Si and Fe-rich lamellar and acicular β-Fe and π-Fe intermetallic phases.
- Micro cracks, cleavage planes, pits and ridge-like structures were detected on the fracture surface observed after tensile tests. These microstructures contributed to the mechanical strength of the alloy and affected the fracture behavior.
- During the drilling process of the alloy, the enhance in *V* caused a decrease in *Fz, Ra* and *Mz* values, but the enhance in *f* increased the values of these indicators.
- BUE was highly formed especially at parameters i.e., *V*: 75 m/min and *f*: 0.25 mm/rev, and it reduced the lowest level at *V*: 125 m/min and *f*: 0.05 mm/rev. The reduce in BUE formation contributed to the improve in machining performance as well as better smoothness of the workpiece surface.
- Scratches, serration, cracks and perforation occurred on the chips during drilling. It was observed that shorter and more brittle chips were formed at high *V*. This situation shows that the effects of chip formation on the cutting tool and material at high *V* differ.
- According to ANOVA analysis, it was point out that the *V* and *f* were statistically important on *Fz, Ra* and *Mz* at 95% confidence level. R^2 correlation coefficients were calculated as 99.93% for *Fz*, 96.20% for *Ra* and 98.68% for *Mz*, which shows that the models made high accuracy predictions.
- As a result of the optimization performed with RSM, the most suitable cutting parameters for minimum *Fz, Ra* and *Mz* values were marked as *V*: 125 m/min and *f*: 0.05 mm/rev.
- In the analyses performed with ANN, the most suitable network structures for *Fz, Ra* and *Mz* were determined as 2-5-1, 2-10-1 and 2-8-1, respectively. ANN presented better predictions having lower error rates compared to RSM method.

As per findings of the paper, several suggestions are recommended as follows: First, comparative studies of different alloy compositions can be performed to obtain more information about the mechanical properties and machinability characteristics. Furthermore, the impacts of various cutting tool geometries and surface coatings during the drilling can be investigated, thus optimizing the cutting tool performance. While long-term performance analyses provide information on the durability of the machined products, material behaviors can be studied in more detail using simulation methods such as finite element analysis. Integration of advanced manufacturing technologies, especially methods such as 3D printing, can develop innovative approaches in material design. Finally, the environmental impacts of these processes should be evaluated, and sustainable manufacturing practices should be encouraged.

CRediT authorship contribution statement

Şenol Bayraktar: Supervision, Conceptualization, Methodology, Investigation, Writing – original draft, Writing – review & editing. **Cem Alparslan:** Investigation, Visualization, Software, Methodology. **Nurten Salihoğlu:** Investigation, Methodology, Visualization. **Murat Sarıkaya:** Methodology, Conceptualization, Writing – review & editing, Validation.

Declaration of competing interest

The authors declare that they have no known competing financial interests or personal relationships that could have appeared to influence the work reported in this paper.

Acknowledgements

The authors would like to thank TÜBİTAK for their support with Project No: 221M064. Additionally, this study has been supported by the Recep Tayyip Erdoğan University Development Foundation (Grant

number: 02024009018075).

Murat Sarıkaya acknowledges the Polish National Agency for Academic Exchange (NAWA) under the Ulam Programme (Grant No. BPN/ULM/2023/1/00035).

References

[1] Grosselle F, Timelli G, Bonollo F. Doe applied to microstructural and mechanical properties of Al–Si–Cu–Mg casting alloys for automotive applications. Mater Sci Eng, A 2010;527:3536–45. https://doi.org/10.1016/j.msea.2010.02.029.
[2] Li H, Li X. The present situation and the development trend of new materials used in automobile lightweight. Appl Mech Mater 2012;189:58–62. https://dx.doi.org/10.4028/www.scientific.net/AMM.189.58.
[3] Mohamed AMA, Samuel FH, Al kahtani S. Influence of Mg and solution heat treatment on the occurrence of incipient melting in Al–Si–Cu–Mg cast alloys. Mater Sci Eng, A 2012;543:22–34. https://doi.org/10.1016/j.msea.2012.02.032.
[4] Callegari B, Lima TN, Coelho RS. The influence of alloying elements on the microstructure and properties of Al-Si-based casting alloys: a review. Metals 2023;13. https://doi.org/10.3390/met13071174.
[5] Beroual S, Boumerzoug Z, Paillard P, Borjon-Piron Y. Effects of heat treatment and addition of small amounts of Cu and Mg on the microstructure and mechanical properties of Al-Si-Cu and Al-Si-Mg cast alloys. J Alloys Compd 2019;784:1026–35. https://doi.org/10.1016/j.jallcom.2018.12.365.
[6] Zhou P, Wang D, Nagaumi H, Wang R, Zhang X, Li X, et al. Microstructural evolution and mechanical properties of Al-Si-Mg-Cu cast alloys with different Cu contents. Metals 2023;13. https://doi.org/10.3390/met13010098.
[7] Aziz AM, Omar MZ, Samat S, Mohamed IF, Sajuri Z, Baghdadi AH. Microstructural and tensile behavior of a thixoformed Al–Si–Cu–Mg given T5 and T6 heat treatments tested at room and elevated temperatures. Int J Metalcast 2024;18:2343–56. https://doi.org/10.1007/s40962-023-01155-x.
[8] Alparslan C, Bayraktar Ş. An experimental study on microstructural, mechanical and machinability properties of as-cast and heat-treated Al-7Si-Mg alloy. Silicon 2024;16:3971–85. https://doi.org/10.1007/s12633-024-02968-z.
[9] Kamatchi Hariharan M, Rajkamal MD, Ravikumar K, Sheik Mohammed M. Investigation on effect of TiN, TiAlN & DLC-triple layer coated carbide tool in machining of Al-Si 4032 alloy. Mater Today Proc 2022;59:39–46. https://doi.org/10.1016/j.matpr.2021.10.197.
[10] Alparslan C, Bayraktar Ş. Experimental research and optimization based on response surface methodology on machining characteristics of cast Al-7Si-0.6 Mg alloy: effects of cutting parameters and heat treatment. Measurement 2024;236:115111. https://doi.org/10.1016/j.measurement.2024.115111.
[11] Jing L, Niu Q, Zhan D, Li S, Yue W. Predictive modeling of surface roughness and feed force in Al-50wt% Si alloy milling based on response surface method and various optimal algorithms. Arabian J Sci Eng 2023;48:3209–25. https://doi.org/10.1007/s13369-022-07114-8.
[12] Bhushan RK. GA approach for optimization of parameters in machining Al alloy SiC particle composite for minimum cutting force. Journal of Alloys and Metallurgical Systems 2023;1:100002. https://doi.org/10.1016/j.jalmes.2023.100002.
[13] Bayraktar Ş, Turgut Y. Effects of WEDM and AWJ cutting methods on induction motor efficiency and total magnetic losses: experimental design and response surface methodology. Measurement 2023;221:113548. https://doi.org/10.1016/j.measurement.2023.113548.
[14] Abd-Elwahed MS. Drilling process of GFRP composites: modeling and optimization using hybrid ANN. Sustainability 2022;14. https://doi.org/10.3390/su14116599.
[15] Kolesnyk V, Peterka J, Alekseev O, Neshta A, Xu J, Lysenko B, et al. Application of ANN for analysis of hole accuracy and drilling temperature when drilling CFRP/Ti alloy stacks. Materials 2022;15. https://doi.org/10.3390/ma15051940.
[16] Goel A, Goel AK, Kumar A. Performance analysis of multiple input single layer neural network hardware chip. Multimed Tool Appl 2023;82:28213–34. https://doi.org/10.1007/s11042-023-14627-3.
[17] Sharkawy A-N, Ameen AG, Mohamed S, Abdel-Jaber GT, Hamdan I. Design, assessment, and modeling of multi-input single-output neural network types for the output power estimation in wind turbine farms. Automation 2024;5:190–212. https://doi.org/10.3390/automation5020012.
[18] Bayraktar Ş, Alparslan C, Salihoğlu N, Sarıkaya M. The impact of heat treatment process on the drilling characteristics of Al–5Si–1Cu–Mg alloy produced by sand casting. J Mater Res Technol 2024;33:2764–72. https://doi.org/10.1016/j.jmrt.2024.10.010.
[19] Mrówka-Nowotnik G, Sieniawski J. Microstructure and mechanical properties of C355. 0 cast aluminium alloy. Arch Materi Sci Eng 2011;47:85–94.
[20] Bayraktar Ş, Demir O. Processing of T6 heat-treated Al-12Si-0.6Mg alloy. Mater Manuf Process 2020;35:354–62. https://doi.org/10.1080/10426914.2020.1732412.
[21] Pathak BN, Sahoo KL, Mishra M. Effect of machining parameters on cutting forces and surface roughness in Al-(1-2) Fe-1V-1Si alloys. Mater Manuf Process 2013;28:463–9. https://doi.org/10.1080/10426914.2013.763952.
[22] Dwivedi SP, Kumar S, Kumar A. Effect of turning parameters on surface roughness of A356/5% SiC composite produced by electromagnetic stir casting. J Mech Sci Technol 2012;26:3973–9. https://doi.org/10.1007/s12206-012-0914-5.
[23] Yücel A, Yıldırım ÇV, Sarıkaya M, Şirin Ş, Kıvak T, Gupta MK, et al. Influence of MoS2 based nanofluid-MQL on tribological and machining characteristics in turning of AA 2024 T3 aluminum alloy. J Mater Res Technol 2021;15:1688–704. https://doi.org/10.1016/j.jmrt.2021.09.007.
[24] Sethupathy A, Shanmugasundaram N. Prediction of cutting force based on machining parameters on AL7075-T6 aluminum alloy by response surface methodology in end milling. Mater Werkst 2021;52:879–90. https://doi.org/10.1002/mawe.202000086.
[25] Carrilero MS, Bienvenido R, Sánchez JM, Álvarez M, González A, Marcos M. A SEM and EDS insight into the BUL and BUE differences in the turning processes of AA2024 Al-Cu alloy. Int J Mach Tool Manufact 2002;42:215–20. https://doi.org/10.1016/S0890-6955(01)00112-2.
[26] Nouari M, List G, Girot F, Géhin D. Effect of machining parameters and coating on wear mechanisms in dry drilling of aluminium alloys. Int J Mach Tool Manufact 2005;45:1436–42. https://doi.org/10.1016/j.ijmachtools.2005.01.026.
[27] Cotterell M, Byrne G. Dynamics of chip formation during orthogonal cutting of titanium alloy Ti–6Al–4V. CIRP Annals 2008;57:93–6. https://doi.org/10.1016/j.cirp.2008.03.007.
[28] Farid AA, Sharif S, Idris MH. Surface integrity study of high-speed drilling of Al–Si alloy using HSS drill. Proc Inst Mech Eng B J Eng Manuf 2011;225:1001–7. https://doi.org/10.1177/2041297510393642.
[29] Bayraktar Ş, Pehlivan G. Machinability characteristics in Zn-40Al alloy: the effect of addition of copper and silicon and optimization of cutting parameters using response surface methodology. J Alloys Compd 2024;1010:178013. https://doi.org/10.1016/j.jallcom.2024.178013.
[30] Bayraktar Ş, Afyon F. Machinability properties of Al–7Si, Al–7Si–4Zn and Al–7Si–4Zn–3Cu alloys. J Braz Soc Mech Sci Eng 2020;42:1–12. https://doi.org/10.1007/s40430-020-02281-x.
[31] Şencan ÇA, Yağmur S, Kavak N, Küçüktürk G, Şeker U. The effect of minimum quantity lubrication under different parameters in the turning of AA7075 and AA2024 aluminium alloys. Int J Adv Manuf Technol 2016;84:2515–21. https://doi.org/10.1007/s00170-015-7878-4.
[32] Alparslan C, Bayraktar Ş. Tool wear in machining of wrought and cast aluminium alloys: literature review. Manuf Technol Appl 2021;2:34–46. https://doi.org/10.52795/mateca.1008145.